PAPER

Check for updates

Preparation of one-dimensional SnO$_2$–In$_2$O$_3$ nano-heterostructures and their gas-sensing property

Hongzhi Shen, [iD] *[a] Liang Li[b] and Dapeng Xu*[b]

Herein, we employ a combination of electrospinning and hydrothermal approaches to synthesize 1D SnO$_2$–In$_2$O$_3$ nano-heterostructures with a series of morphological evolutions. Through variations in the mole ratio of Sn^{4+} and In^{3+} ions in hydrothermal condition, several 1D SnO$_2$–In$_2$O$_3$ heterogeneous morphologies have been realized. The proposed growth mechanism for 1D nano-heterostructures is expected to be a nucleation-growth process. In$_2$O$_3$ nanofibers, as templates, provide numerous nucleation sites for the growth of SnO$_2$ nanostructures. As the Sn^{4+} concentration increases, the SnO$_2$ nucleus can start to grow from the surface of In$_2$O$_3$ template and extend out along the lateral direction until adjacent grains begin to be connected, forming morphological evolutions. The sensor of SnO$_2$ nanocylinders, grown on In$_2$O$_3$ nanofibers (SI-3 sample), exhibits highest response value at optimal operating temperature. The sensor based on SI-3 sample displays quicker recovery capability towards ethanol gas. A rapid recovery rate can be ascribed to the spillover effect and high surface area. The gas-sensing mechanism of 1D SnO$_2$–In$_2$O$_3$ nano-heterostructures has been discussed.

Introduction

One-dimensional (1D) semiconducting metal-oxide nano-structures have gained considerable attention as flammable and toxic gas detectors for application in environment, oil, chemicals and mining *etc.*[1] High sensing performance depends not only on the intrinsic property of the material itself, but also on the special structural parameters, such as high specific surface and large porosity.[2] 1D metal-oxide gas sensors, with small particle size and large surface area, make it easy to promote interaction between the testing gas molecules and the adsorbed oxygen molecules. Electrospinning technique is a simple and versatile route to prepare inorganic nanofibers. Nanofibers because of their interesting features, such as surface-to-volume ratio, high surface area, microporosity, and nonwoven structure, provide numerous opportunities to design novel carrier systems for gas-sensing reactions.[3] However, single-component one-dimensional (1D) nanomaterials have been unsatisfactory, increasing gas monitoring demands in complex conditions. To efficiently enhance gas detection capability, some studies utilize electrospun nanofibers as hard template to fabricate complex 1D nanostructures *via* suitable and compatible growth methods, in which second component is grown directly on a framework of nanowires or nanofibers. These 1D nanosized heterostructures as gas sensors have the following advantage: the assembly of secondary nanostructures on nanofibers' surface not only provides numerous active sites and surface atoms for gas diffusion, but also improves response and recovery activities for testing gas. On the other hand, the formation of heterostructures with favorable band alignment can lead to novel interface effects and a functional integration of the properties of both the materials. In contrast with single-component nanofibers, multicomponent 1D nano-heterostructures have been shown to possess superior property or new functionality.

As a new type of gas-sensing material, indium oxides (In$_2$O$_3$, E_g = 3.55–3.75 eV) have been intensively investigated due to good conductivity and high gas response and low toxicity.[4,5] In$_2$O$_3$ nanomaterials with various morphologies exhibit higher sensitivity and selectivity for oxidizing or reducing gas compared to conventional gas-sensing material like SnO$_2$, Fe$_2$O$_3$ and ZnO *etc.*[6–8] Particularly, In$_2$O$_3$-based composite nanostructures produced by surface modification or doping have shown excellent enhancement in gas-sensing activity over their components. Recently, some researches made several attempts to extend response and recovery properties of In$_2$O$_3$-based nanostructures, such as doping with metal ions,[9–11] surface coating[12] and seeding secondary growth.[13] Among these attempts, coupled In$_2$O$_3$ nanostructure with traditional semiconducting oxides to form 1D heterostructures had been a novel approach for improving gas-sensing performance. For instance, In$_2$O$_3$/a-Fe$_2$O$_3$ heterostructure nanotubes,[14] CuO–In$_2$O$_3$ core–shell nanowires,[15] In$_2$O$_3$/TiO$_2$ composite nanofibers,[16,17] and In$_2$O$_3$/ZnO core–shell nanorods[18] were investigated. Although a few syntheses

[a]College of Physics, Beihua University, Jilin 132013, P. R. China. E-mail: shen061288@sina.com

[b]College of Physics, Jilin University, Changchun 130000, P. R. China

This journal is © The Royal Society of Chemistry 2017

of 1D nano-heterostructure with In_2O_3 component have been reported in recent years, In_2O_3 has only acted as a secondary component on nano-heterostructure surface. To date, In_2O_3 has never been used as a major component to fabricate multi-component 1D nano-heterostructure. Tin dioxide (SnO_2) is the most important material for use in gas sensing applications.[19] It is the dominant choice for solid state gas detectors in domestic, commercial and industrial settings due to the low operating temperatures, high sensitivities, mechanical simplicity of sensor design and low manufacturing costs.[20,21] If the SnO_2 grains are deposited onto the surface of 1D In_2O_3 nanostructures, this new sensing system will effectively reveal the connection between the microstructure and the gas-sensing performance. In this study, the SnO_2 nanoparticles decorated In_2O_3 nanofibers were prepared by a two-step method: electrospinning combined with hydrothermal methods. We have carefully evaluated the formation mechanism of SnO_2–In_2O_3 1D nano-heterostructures, and then depicted the gas sensing difference between the In_2O_3 nanofibers and SnO_2–In_2O_3 1D nano-heterostructures to identify the parameters that influence the gas sensing performance.

Experimental

The synthesis of In_2O_3 nanofibers

The raw materials were $In(NO_3)_3$, polyvinylpyrrolidone (PVP), dimethylformamide (DMF) and ethanol. In a typical procedure, 1 g of polyvinylpyrrolidone (PVP, $M_w = 1\ 300\ 000$) powder was dissolved in the mixture of 4.5 g of ethanol and 4.5 g of dimethylformamide (DMF). Subsequently, 3 mmol of $In(NO_3)_3$ was added to the above solution and stirred for 2 h to form transparent and homogeneous precursor solution.

The precursor solution was placed in a 5 ml glass syringe equipped with a stainless steel needle. A positive electrode was connected to the steel needle tip while a piece of aluminum foil covered collector worked as the negative plate. Distance between the needle tip and the collector was fixed at 10 cm, and electrospun voltage was controlled at 13 kV. In_2O_3 nanofibers were obtained by calcination of the precursor nanofibers at 600 °C for 2 h in air.

The synthesis of 1D SnO_2–In_2O_3 nano-heterostructures

SnO_2 nanostructures were deposited on the surface of In_2O_3 nanofibers by hydrothermal methods. In a typical procedure, 20 mg of In_2O_3 nanofibers were put into 30 ml of deionized water to form the suspension liquid. Different amounts of $SnCl_4$ (the mole ratio of elements, $Sn^{4+} : In^{3+} = 1 : 10, 1 : 5$ and $1 : 2.5$) were added into the above solution. Then, aqueous ammonia solution was added dropwise until pH of the solution was 10. After being ultrasonically treated, the mixture solution was transferred into Teflon-lined stainless steel autoclave of 50 ml capacity and sealed tightly. The autoclave was maintained at 140 °C for 2 h in an oven, and then cooled naturally to room temperature, as summarized in Table 1. The obtained products were washed with deionized water, filtered and dried in an oven at 80 °C for 12 h.

The gas sensing measurement

In the gas-sensing measurement, ethanol was employed as the target gas. The as-obtained 1D SnO_2–In_2O_3 nano-heterostructures were mixed with the appropriate amount of deionized water in an agate mortar to produce paste, which were subsequently brushed onto the alumina ceramic tubes. These tubes were dried under IR light for several minutes in air and calcinated at 200 °C for 1 h. Fig. 1 shows a schematic of the as-prepared sensor. Each ceramic tube is attached with a pair of gold electrodes, which were used for linking the tube with the gas detecting device (each electrode was connected to two Pt wires). A Ni–Cr heating wire was inserted in the tube as a resistor to adjust the operating temperature. The gas sensors were aged at 300 °C for 240 h in air to enhance stability and repeatability.

In general, the gas-sensing performances were tested using an intelligent gas-sensing test system (CGS-8, China). The as-prepared sensors were placed into a closed glass chamber, and the suitable concentration of ethanol gas was injected inside the chamber for measurement of the sensing performance. The gas sensors were used as a load resistor in measuring the electric circuit of the gas sensor. When a suitable amount of ethanol gas was injected into the chamber, the resistance of the sensor changed. By regulating the operating temperature, the resistance of samples was measured in air and in ethanol gas. The sensor response was defined as $S = R_a/R_g$, where R_a was the resistance of the sensor in air and R_g was the resistance in ethanol gas. The response time and recovery time were described as the time taken by the sensor to achieve 90% of the total resistance change after sensor was exposed to ethanol gas and air, respectively.

Characterization

Structural analyses of the samples were carried out by X-ray diffraction (XRD) using an X-ray diffractometer (Rigaku D/max-2500) with Cu Kα radiation ($\lambda = 1.5406$ Å) and a step size of 0.02°. The morphology and surface of the nanofibers was inspected using field emission-scanning electron microscopy (FE-SEM JSM-6700F Japan) and high resolution transmission electron microscopy (HRTEM Tecnai G2 F20 America). The composition analysis of samples was performed using energy dispersive X-ray (EDX) spectroscopy combined with scanning electron microscopy (SEM). The specific surface area of the samples were analyzed by Brunauer Emmett Teller measurements (BET JW-BK100A China).

Results and discussions

The structure and morphology

The morphologies of three nano-heterostructures were observed by SEM, as illuminated in Fig. 2. Fig. 2a shows that the obtained nanofibers are rough and flexible with an average diameter of approximately 200 nm. Enlarged images (Fig. 2b) show that nanofibers surface is covered by a number of bulge-like spherical particles. On increasing the mole ratio of Sn/In, these bulges evolved into regular nanograins on the surface.

Table 1 Experimental conditions for the preparation of three SnO_2–In_2O_3 samples

Sample no.	Starting Sn/In mole ratio	Hydrothermal temperature and time	Secondary SnO_2 size (nm)	Morphology
SI-1	1 : 10	140 °C, 2 h	40	SnO_2 particles grown on In_2O_3 nanofibers
SI-2	1 : 5	140 °C, 2 h	60	SnO_2 nanograins grown on In_2O_3 nanofibers
SI-3	1 : 2.5	140 °C, 2 h	80	SnO_2 nanocylinders grown on In_2O_3 nanofibers
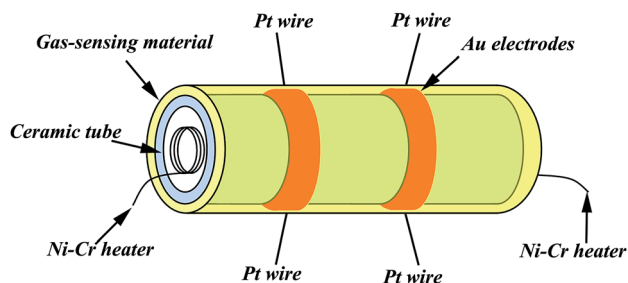
Fig. 1 Schematic diagram of the gas sensor.

These nanograins have diameters of about 50–70 nm, and their distributions are relatively uniform (Fig. 2c and d). If the starting Sn/In ratio is further increased to 4 times, numerous nanocylinders instead of regular nanograins grow on the surface of the In_2O_3 nanofibers (Fig. 2e and f). It is demonstrated that additions of $SnCl_4$ make it possible to synthesize 1D

nano-heterostructure with cylinders as large as 80 nm on the heterostructure surface. Fig. 2g shows that the pristine In_2O_3 nanofibers have diameters of about 200 nm, and the surface is relatively smooth without any secondary nanostructures. Fig. 2i is a typical HRTEM image recorded from the corresponding surface area in SI-3 samples. Well-resolved lattice fringes can be clearly observed on the surface and in the internal regions. The spacing of lattice plane of surface nanostructures is approximately 0.336 nm, which agrees well with the (110) lattice index of SnO_2. Lattice spacing of internal regions is about 0.414 nm, ascribed to (211) crystal planes of cubic In_2O_3. To find the exact chemical composition of the surface nanostructures, multiple spot analysis of the surface area were carried out using Energy-Dispersive Spectrometer (EDS). Fig. 3 shows the one on SI-3 sample with two unique points identified. The resulting spectra reveal that all the spots represent the three elements of In, O, and Sn detected in the inspection field, with In being the most abundant. Note that the content of Sn element has great difference in results of the two inspection spots. Compared to
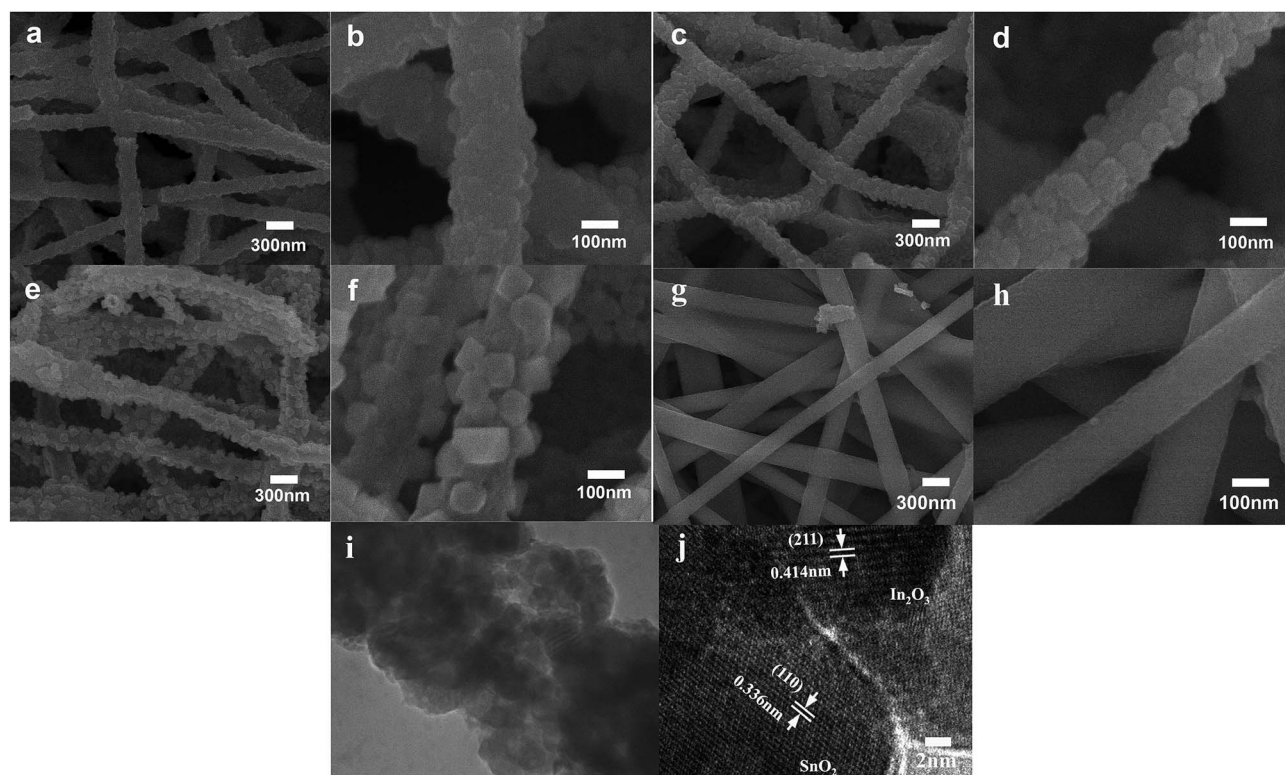
Fig. 2 SEM and TEM images of 1D SnO_2–In_2O_3 nano-heterostructures: (a) low and (b) high magnification Si-1 samples; (c) low and (d) high magnification Si-2 samples; (e) low and (f) high magnification Si-3 samples; (g) low and (h) high magnification In_2O_3 nanofibers (i) different magnification tem images of Si-3 samples; (j) HRTEM images of Si-3 samples.
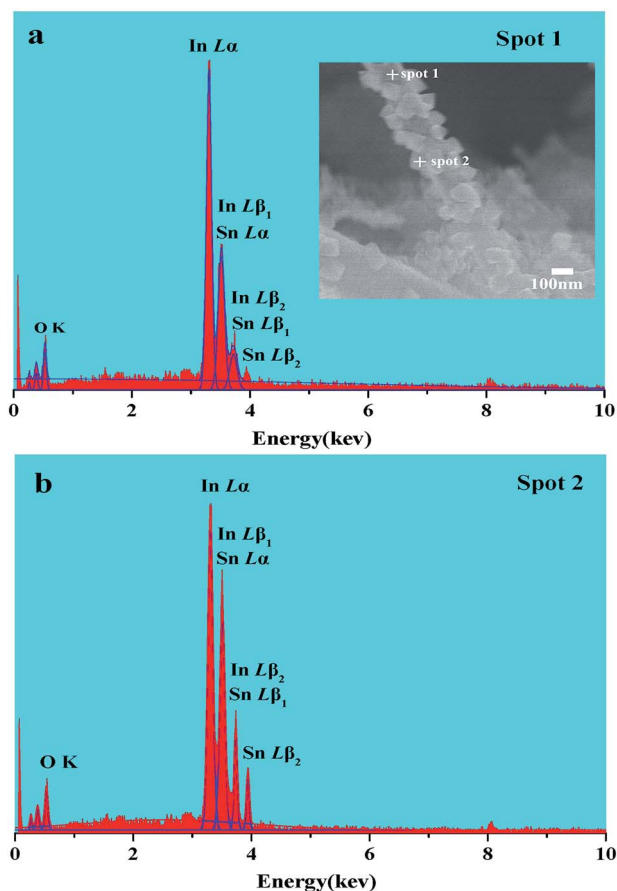
Fig. 3 (a, b) EDX spectra taken from spot 1 and 2 in the inset.

the measuring spots, it is found that the percentage of Sn element on surface nanocylinders (spot 3) is slightly higher than that on other field (spot 1 and spot 2). This indicates that secondary component grown on the nanofibers consists of SnO_2 crystal grains.

In order to study the crystal structure of samples, overall phase purity and crystal structure of all the samples (SnO_2,
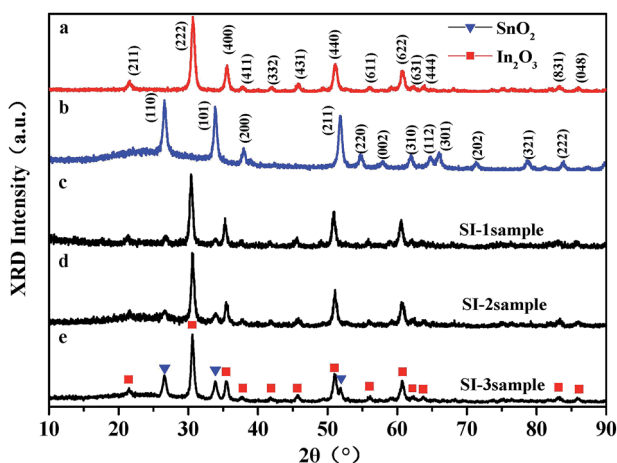

Fig. 4 XRD patterns of (a) In_2O_3 nanofibers, (b) SnO_2 nanoparticles, (c) Si-1 samples, (d) Si-2 samples and (e) Si-3 samples.

In_2O_3, SI-1, SI-2, and SI-3) have been analyzed by XRD, as shown in Fig. 4. All the diffraction peaks in the pattern of pure In_2O_3 nanofibers can be indexed to cubic structure (JCPDS no. 71-2194). For 1D nano-heterostructure, XRD pattern shows that there are some additional diffraction peaks other than the In_2O_3 peaks. These peaks at $2\theta = 26.7°, 33.9°, 37.6°, 51.7°$ match with SnO_2 phase with rutile structure, which is in agreement with the standard card (JCPDS no. 084576). With an increase in the SnO_2 grain size, the intensity of two characteristic peaks assigned at SnO_2 increase continuously. Combining SEM and HRTEM results, it is demonstrated that nanostructures grown on the surface of In_2O_3 nanofibers possess the rutile structure of SnO_2 phase. Several heterogeneous morphologies have been acquired by changing the conditions of synthesis. This indicates that the 1D SnO_2–In_2O_3 nano-heterostructures with a series of morphological evolutions have been successfully prepared *via* electrospinning, followed by the hydrothermal treatment.

The proposed growth mechanism for the formation of 1D SnO_2–In_2O_3 nano-heterostructures can be explained in terms of the chemical reaction and crystal growth, as shown in Fig. 5. In our experiment, it is observed that the shape of the as-prepared samples changes by increasing the mole ratio of Sn^{4+} and In^{3+} ions. According to previous reports,[22,23] the chemical reaction for the growth of secondary SnO_2 nanostructures is proposed as follows:[24]

$$Sn^{4+} + 6OH^- \rightarrow [Sn(OH)_6]^{2-}$$

$$[Sn(OH)_6]^{2-} \rightarrow SnO_2 + H_2O + OH^-$$
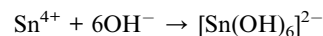
Tetravalent tin Sn^{4+} ions easily produce $Sn(OH)_6^{2-}$ anions in excess of alkaline solution. As the reaction temperature rises, the $Sn(OH)_6^{2-}$ ions decompose into SnO_2. From the crystallization point of view, the growth of an alkaline solution of SnO_2 nanostructures is expected to be a nucleation-growth process. Electrospun In_2O_3 nanofibers with a rough surface provide numerous nucleation sites for the growth of SnO_2 nanostructures. Moreover, the interface regions of nanofibers are also related to a large number of unsaturated dangling bonds, which are beneficial to promote the heterogeneous nucleation of SnO_2 nanostructure. These SnO_2 nuclei with high surface energy are still in an unstable thermodynamic state. In this case, the nucleus continues to grow as the $Sn(OH)_6^{2-}$ ions resolve it in solution and then generate a different morphology of 1D nano-heterostructures.

Recently, some groups used nanofibers as templates available to control the nucleation.[25,26] The Sn^{4+} concentration in hydrothermal solution affects the growth of the SnO_2 size directly, and it is clear that the morphology of secondary SnO_2 undergoes a dramatic evolution from nanoparticles to nanocylinders. A consequence of SnO_2 nanograins' growth can be attributed to a synergistic effect of the Ostwald-ripening process.[27] In the process, numerous small SnO_2 crystals formed initially slowly disappear, except for a few that grow larger, at the expense of the small crystals. The smaller crystals act as fuel for the growth of bigger crystals. In the early stage of condensation, the SnO_2 nucleates at a different position along
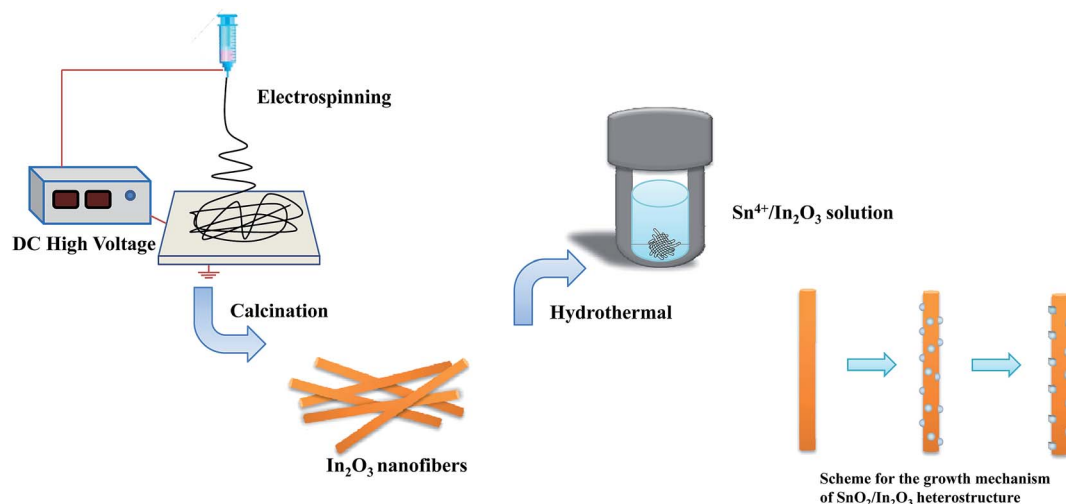
Fig. 5 The proposed formation mechanism of 1D SnO$_2$–In$_2$O$_3$ nano-heterostructures.

the indium oxide template or backbone. After a long-time in SnO$_2$ condensation, SnO$_2$ shows a tendency to condense on the surface of larger particles. In$_2$O$_3$ nanofibers act as a reservoir for the accommodation of SnO$_2$ nanoparticles and offer a template during the hydrothermal synthesis.

Gas-sensing property for alcohol

It is well-known that there are several important factors that can determine the gas-sensing performance of 1D SnO$_2$–In$_2$O$_3$ nano-heterostructures for detecting a given gas, which are as follows: optimal operating temperature, sensitivity, response and recovery time *etc.* Fig. 6a shows the responses of the as-prepared samples, In$_2$O$_3$ nanofibers and SnO$_2$ powders to 100 ppm ethanol at operating temperatures from 175 to 300 °C. It is found that the responses of the as-prepared samples have a similar trend that first increases and then gradually decreases with increase of operating temperature. The optimal operating temperature for most samples was 250 °C, and SnO$_2$ attained its maximum value at 300 °C. As a comparison, the sensor of SnO$_2$ nanocylinders grown on In$_2$O$_3$ nanofibers (SI-3 sample) exhibited the highest response value at optimal operating temperature. The result indicates that the response reaches its maximum value of 15.4 at 250 °C, which is 1.5 times higher than response value of In$_2$O$_3$ nanofibers. Fig. 6b displays the responses of the as-prepared samples to different ethanol concentrations at optimal operating temperature (250 °C). The gas sensitivity of obtained samples increases sharply in the range from 10 to 5000 ppm and then gradually reaches a saturated value at the ethanol concentration of 10 000 ppm. Pure SnO$_2$ shows the best gas sensing activity, up to 10 000 ppm ethanol at 250 °C. This indicates that deposited SnO$_2$ is very useful for the improvement of gas response rate on 1D hetero-structure surface.

In addition, rapid response/recovery times are also important parameters to measure the gas-sensing performance of the material. Fig. 7 shows the response transient of the sensor based on the as-prepared samples, SnO$_2$ powders and In$_2$O$_3$
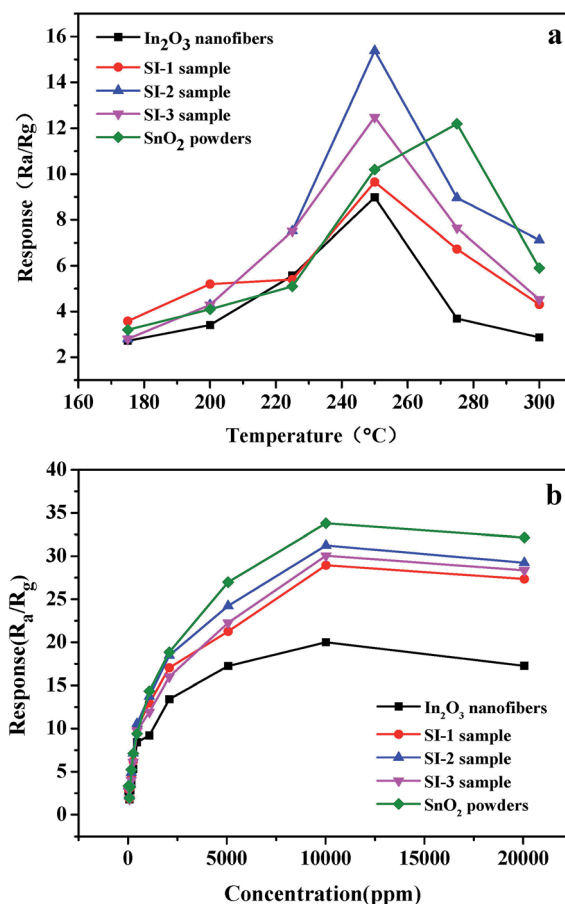

Fig. 6 (a) Gas response of the In$_2$O$_3$ nanofibers, SnO$_2$ powders, Si-1 sample, Si-2 sample and Si-3 sample based sensor toward 100 ppm ethanol at series of operating temperatures ranging from 125 to 300 °C, respectively; (b) gas response of the In$_2$O$_3$ nanofibers, SnO$_2$ powders, Si-1 sample, Si-2 sample and Si-3 sample based sensor toward 250 °C at different ethanol concentration.
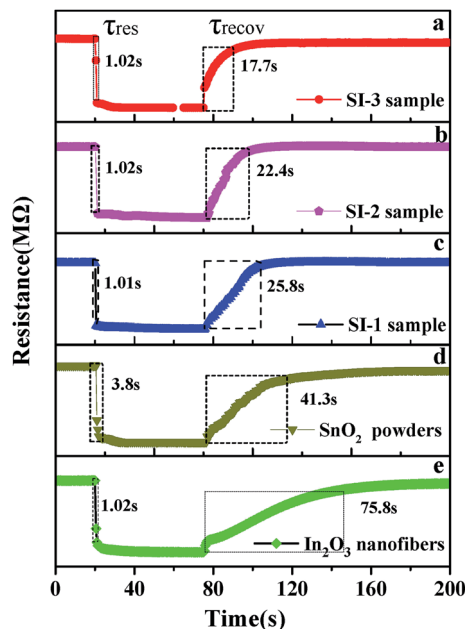
Fig. 7 (a–e) Response and recovery time of the Si-3 sample, Si-2 sample, Si-1 sample, SnO_2 powders and In_2O_3 nanofibers to 100 ppm ethanol at 250 °C.

nanofibers to 100 ppm ethanol at 250 °C. It can be observed that response curve starts a precipitous decline and reaches a stable state when the five sensors are exposed to ethanol. The response times of three sensors are 1.02 s (SI-3), 1.01 s (SI-2), 1.02 s (SI-1), 3.8 s (SnO_2) and 1.02 s (In_2O_3), respectively. After exposure to air, the recovery times are 17.7 s, 22.4 s, 25.8 s, 41.3 s and 75.8 s for SI-3, SI-2, SI-1, SnO_2 and In_2O_3, respectively. As can be observed, response time does not vary greatly when several sensors are exposed to 100 ppm ethanol. In contrast, the recovery times are significantly different for three sensors. Some researchers[28] reported that the response and recovery times of as-prepared In_2O_3–SnO_2 composites to 100 ppm ethanol at 250 °C are about 15 s and 60 s, respectively. As compared with previous reports, SnO_2 deposited In_2O_3 nanofibers exhibit better gas sensitivity. The rapid response rates, particularly recovery time, are remarkable. It is noteworthy that the sensor based on SI-3 sample displays quicker recovery capability toward ethanol gas.

Gas-sensing mechanism of 1D SnO_2–In_2O_3 nano-heterostructures

According to the above results, the sensor based on 1D SnO_2–In_2O_3 nano-heterostructures show outstanding ethanol gas sensitivity and response transient compared with pure 1D In_2O_3 nanostructures. Fig. 8 shows nitrogen adsorption–desorption isothermal curves of pure In_2O_3 and SI-3 samples. BET analysis reveals that the surface area of SI-3 samples is 47.3 m³ g⁻¹, which is much larger than that of pure In_2O_3 (21.4 m³ g⁻¹) nanofibers. This illustrates that the surface area of nanofibers increases significantly after deposition of SnO_2. The characteristics of gas sensors depend on the change in the surface
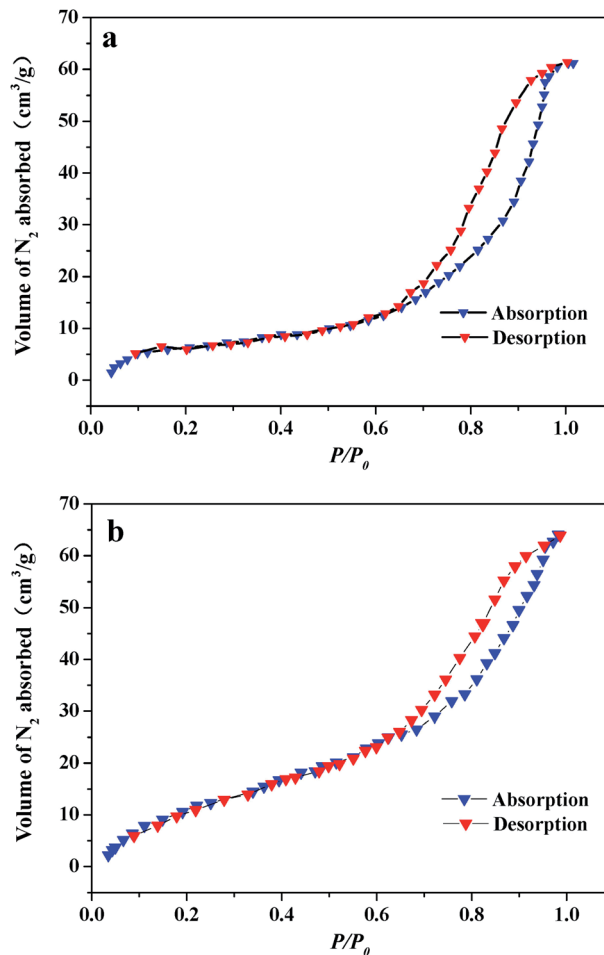

Fig. 8 Nitrogen adsorption–desorption isothermal curves of (a) pure In_2O_3 nanofibers, nitrogen adsorption–desorption isothermal curves of (b) Si-3 sample.

resistance in the presence of gas, and adsorption/desorption behavior between gas molecules and surfaces have a direct impact on surface resistance of heterostructures. SnO_2-deposited In_2O_3 nanofibers have a high specific surface area, which not only provides a large adsorption region for the oxygen species and target gas but also promotes the interaction between the oxide surface and the gas molecules.[29] Secondary nanostructures on the surface of nanofibers, SnO_2 nanocylinders, are used to modulate electric transport of In_2O_3 nanofibers in order to improve the gas-sensing property of individual semiconductor sensors.[30] Gas-sensing mechanism of 1D SnO_2–In_2O_3 nano-heterostructures is shown in Fig. 9. After being exposed to air, oxygen will be adsorbed on the surface of the SnO_2 nanostructures and then trap electrons from the conduction band to form ionized oxygen species (O_{ads}^-, O^{2-}, and O_2^-), resulting in increase of barrier height at the interface between SnO_2 nanostructure and In_2O_3 nanofibers. As a consequence, this tends to increase the resistance of 1D heterostructures. When the obtained 1D heterostructures are exposed to target gas, ethanol molecules react with the absorbed oxygen species, and the trapped electrons are released to the conduction band of SnO_2 and In_2O_3, leading to remarkable changes in
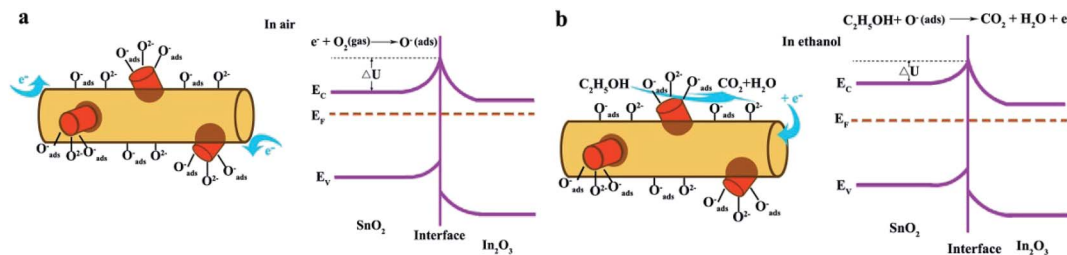
Fig. 9 (a, b) Schematic diagrams of gas-sensing mechanism of 1D SnO$_2$–In$_2$O$_3$ nano-heterostructures in air and ethanol.

electric conductivity because of lower barrier height at the interfaces.

As we mentioned in the results, it is found that recovery rate is observed to increase with increasing of surface size of SnO$_2$. In order to understand gas reaction of special surface nano-structure, it is necessary to consider some surface chemistry concepts. In general, the gas sensing principle depends on the adsorption/desorption behavior between gas molecules and surfaces. Under similar measuring condition (same gas concentration and temperature), adsorption and desorption of gas molecules depends not only on the intrinsic property of the adsorbed gas, but also on the surface structure of sensors. From chemisorption kinetics, the adsorption rate of gas molecules is proportional to the gas concentration and to the number of unoccupied adsorption sites. The rate constant of the desorption process (R_{des}) is given *via* the Arrhenius equation as follows:

$$R_{des} = A_{des} \exp\left(-\frac{E_D}{RT}\right)$$

where A_{des} is the pre-exponential factor, E_D is the activation energy for desorption (which may depend upon the surface coverage and the frequency of the gas molecule-surface bonding), T is the temperature and R is the universal gas constant.[31,32] In some cases, adsorbed gas molecules are chemically bonded to the surface, providing a strong adhesion and limiting desorption. If this is the case, the surface bond of adsorbed molecules can be rapidly cleaved by enhancing activation energy. In 1D nano-heterostructure-based gas sensors, the surface area is enlarged because of the growth of secondary SnO$_2$ nanostructures, resulting in increase of the number of adsorption sites. When ethanol gas is injected, 1D SnO$_2$–In$_2$O$_3$ nano-heterostructures enable the gas-sensing layer to possess a larger internal space compared with regular nanofibers. Once ethanol gas is removed, the residual ethanol molecules require activation energy supplied either thermally or by photoexcitation to achieve desorption process, which often requires a chemical reaction to cleave the chemical bonds. One way to accomplish this is to apply a number of electrons to the surface, resulting in either reduction or oxidation of the adsorbed molecule. From the foregoing results, as the size of these particles to fiber surface increases, the desorption rate increases sharply. Combining the deposition and sensing characterization, one concept can be invoked to explain the improvement of nanofiber's desorption rate upon SnO$_2$ deposition. SnO$_2$

nanoparticles are regarded as a catalyst, which activates dissociation of molecular oxygen. The catalytic process increases both quantity of atomic oxygen that can repopulate vacancies on 1D nano-heterostructures surface and rate at which this repopulation occurs, resulting in a cloud of electron withdrawal from the In$_2$O$_3$ to surface. This is called the spillover effect in catalysis.[33,34] As a result, surface-adsorbed oxygen and residual alcohol react rapidly under catalysis of active SnO$_2$ particles, leading to observed improvement in gas recovery effect. In addition, high surface area is helpful for ethanol diffusion and its reaction on the surface. However, the situation for 1D nano-heterostructures is much more complex than the simple 1D nanostructures and further research is needed to be done to explain the desorption reaction mechanisms. In a word, SnO$_2$-deposited In$_2$O$_3$ nanofibers show a significant improvement in gas-sensing activity compared to single component In$_2$O$_3$ nanofibers. In a real application, fast response and recovery rate may be able to deduce whether ethanol leak has occurred in short succession.

Conclusion

1D SnO$_2$–In$_2$O$_3$ nano-heterostructures with a series of morphological evolutions have been successfully synthesized *via* electrospinning, followed by the hydrothermal treatment. Through variations in the mole ratio of Sn^{4+} and In^{3+} ions in hydrothermal condition, several 1D SnO$_2$–In$_2$O$_3$ heterogeneous morphologies have been realized. With an increase in the mole ratio of Sn/In, surface SnO$_2$ morphology changes from nanoparticles to nanograins and further to nanocylinders, and the size increases from 30 nm to about 80 nm. The underlying mechanisms of morphology control for 1D nano-heterostructures is expected to experience a nucleation-growth process. In$_2$O$_3$ nanofibers as templates provide numerous nucleation sites for the growth of SnO$_2$ nanostructures. Sensors based on 1D SnO$_2$–In$_2$O$_3$ nano-heterostructures displayed numerous advantages in terms of greater reliability, high sensitivity to ethanol gas. The sensor of SnO$_2$ nanocylinders grown on In$_2$O$_3$ nanofibers (SI-3 sample) exhibits highest response value at 250 °C. The as-prepared SI-3 sample displays quicker recovery capability towards ethanol gas, which exceeds those reported in literature. The improvement of desorption rate is ascribed to the effect of spillover of atomic oxygen formed catalytically on the SnO$_2$ particles. Due to catalytic activity of the deposited SnO$_2$, surface-adsorbed oxygen and residual alcohol

undergo a rapid oxidation reaction, resulting in the observed reduction in the gas recovery time.

References

1 R. S. Devan, R. A. Patil, J. H. Lin and Y. R. Ma, *Adv. Funct. Mater.*, 2012, **22**, 3326–3370.

2 E. Comini, *Anal. Chim. Acta*, 2006, **568**, 28–40.

3 B. Ding, M. Wang, J. Yu and G. Sun, *Sensors*, 2009, **9**, 1609–1624.

4 A. Gurlo, N. Barsan, U. Weimar, M. Ivanovskaya, A. Taurino and P. Siciliano, *Chem. Mater.*, 2003, **15**, 4377–4383.

5 S. Elouali, L. G. Bloor, R. Binions, I. P. Parkin, C. J. Carmalt and J. A. Darr, *Langmuir*, 2012, **28**, 1879–1885.

6 D. O. K. A. Kolmakov, Y. Lilach, S. Stemmer and M. Moskovits, *Nano Lett.*, 2005, **5**, 667–673.

7 S. G. Leonardi, A. Mirzaei, A. Bonavita, S. Santangelo, P. Frontera, F. Panto, P. L. Antonucci and G. Neri, *Nanotechnology*, 2016, **27**, 075502.

8 S. Roso, F. Güell, P. R. Martínez-Alanis, A. Urakawa and E. Llobet, *Sens. Actuators, B*, 2016, **230**, 109–114.

9 H. Yang, S. Wang and Y. Yang, *CrystEngComm*, 2012, **14**, 1135–1142.

10 L. Liu, T. Zhang, S. Li, L. Wang and Y. Tian, *Mater. Lett.*, 2009, **63**, 1975–1977.

11 Y. D. Zhang, Z. Zheng and F. L. Yang, *Ind. Eng. Chem. Res.*, 2010, **49**, 3539–3543.

12 D. Sanders and U. Simon, *J. Comb. Chem.*, 2007, **9**, 53–61.

13 L. Xu, H. Song, B. Dong, Y. Wang, J. Chen and X. Bai, *Inorg. Chem.*, 2010, **49**, 10590–10597.

14 C. Zhao, G. Zhang, W. Han, J. Fu, Y. He, Z. Zhang and E. Xie, *CrystEngComm*, 2013, **15**, 6491.

15 X. Li, X. Li, N. Chen, X. Li, J. Zhang, J. Yu, J. Wang and Z. Tang, *J. Nanomater.*, 2014, **2014**, 1–7.

16 P. Chen, P. Yao and J. Wang, *The 14th International Meeting on Chemical Sensors*, 2012, pp. 1064–1067.

17 H. Wu, K. Kan, L. Wang, G. Zhang, Y. Yang, H. Li, L. Jing, P. Shen, L. Li and K. Shi, *CrystEngComm*, 2014, **16**, 9116–9124.

18 N. Singh, A. Ponzoni, R. K. Gupta, P. S. Lee and E. Comini, *Sens. Actuators, B*, 2011, **160**, 1346–1351.

19 A. Paliwal, A. Sharma, M. Tomar and V. Gupta, *J. Appl. Phys.*, 2016, **119**, 164502.

20 W. Xu, L. Xia, J. G. Ju, P. Xi, B. W. Cheng and Y. X. Liang, *J. Sol-Gel Sci. Technol.*, 2016, **78**, 353–364.

21 X. Xu, J. Zhuang and X. Wang, *J. Am. Chem. Soc.*, 2008, **130**, 12527–12535.

22 S. Cao, W. Zeng, Z. Zhu and X. Peng, *J. Mater. Sci.: Mater. Electron.*, 2014, **26**, 1820–1826.

23 X. Kuang, T. Liu, D. Shi, W. Wang, M. Yang, S. Hussain, X. Peng and F. Pan, *Appl. Surf. Sci.*, 2016, **364**, 371–377.

24 H. Liu, J. Chen, R. Hu, X. Yang, H. Ruan, Y. Su and W. Xiao, *J. Mater. Sci.: Mater. Electron.*, 2015, **27**, 3968–3973.

25 P. W. Voorhees, *J. Stat. Phys.*, 1984, **38**, 231–252.

26 A. Vomiero, M. Ferroni, E. Comini, G. Faglia and G. Sberveglier, *Nano Lett.*, 2007, **7**, 3553–3558.

27 Z. Jing and J. Zhan, *Adv. Mater.*, 2008, **20**, 4547–4551.

28 Y. Liu, S. Yao, Q. Yang, P. Sun, Y. Gao, X. Liang, F. Liu and G. Lu, *RSC Adv.*, 2015, **5**, 52252–52258.

29 Y. Chen, C. Zhu and T. Wang, *Nanotechnology*, 2006, **17**, 3012–3017.

30 J. R. Dacey, *Ind. Eng. Chem.*, 1965, **57**, 27–33.

31 G. Horz, *Metall. Trans.*, 1972, **3**, 3069–3076.

32 J. K. Rath, S. K. Agarawalla and G. S. Roy, *Researcher*, 2013, **5**, 75–79.

33 A. Kolmakov, D. O. Klenov, Y. Lilach, S. Stemmer and M. Moskovits, *Nano Lett.*, 2005, **5**, 667–673.

34 R. J. Hu, J. Wang and H. C. Zhu, *Acta Phys.-Chim. Sin.*, 2015, **31**, 1997–2004.